

## ARTICLE OPEN



# Attosecond magnetization dynamics in non-magnetic materials driven by intense femtosecond lasers

Ofer Neufeld<sup>1</sup>✉, Nicolas Tancogne-Dejean<sup>1</sup>, Umberto De Giovannini<sup>1,2</sup>, Hannes Hübener<sup>1</sup> and Angel Rubio<sup>1,3</sup>✉

Irradiating solids with ultrashort laser pulses is known to initiate femtosecond timescale magnetization dynamics. However, sub-femtosecond spin dynamics have not yet been observed or predicted. Here, we explore ultrafast light-driven spin dynamics in a highly nonresonant strong-field regime. Through state-of-the-art *ab initio* calculations, we predict that a nonmagnetic material can transiently transform into a magnetic one via dynamical extremely nonlinear spin-flipping processes, which occur on attosecond timescales and are mediated by cascaded multi-photon and spin-orbit interactions. These are nonperturbative nonresonant analogs to the inverse Faraday effect, allowing the magnetization to evolve in very high harmonics of the laser frequency (e.g. here up to the 42nd, oscillating at  $\sim 100$  attoseconds), and providing control over the speed of magnetization by tuning the laser power and wavelength. Remarkably, we show that even for linearly polarized driving, where one does not intuitively expect the onset of an induced magnetization, the magnetization transiently oscillates as the system interacts with light. This response is enabled by transverse light-driven currents in the solid, and typically occurs on timescales of  $\sim 500$  attoseconds (with the slower femtosecond response suppressed). An experimental setup capable of measuring these dynamics through pump-probe transient absorption spectroscopy is simulated. Our results pave the way for attosecond regimes of manipulation of magnetism.

*npj Computational Materials* (2023)9:39; <https://doi.org/10.1038/s41524-023-00997-7>

## INTRODUCTION

Magnetism is one of the most fundamental physical phenomena in nature. It arises from internal spin degrees of freedom of quantum particles<sup>1,2</sup>, and can create complex spin textures, such as skyrmions<sup>3–6</sup> or other magnetic and topological-ordered phases<sup>7–9</sup>. Over the past two decades, immense efforts have been devoted towards the study of ultrafast magnetism, i.e., the manipulation of materials' magnetic structures on femtosecond timescales with ultrashort laser pulses<sup>10–15</sup>. However, despite many years of research, numerous open questions remain regarding the mechanisms and pathways that control ultrafast magnetization dynamics<sup>10–19</sup>. Part of the complexity arises because spin dynamics are often entangled with other processes and interactions (because spin is carried by charged particles that also interact with each other and with other particles), and can also evolve over several orders of magnitudes of timescales ranging from femtoseconds to nanoseconds. For instance, only recently the mechanism through which angular momentum transfers from the spin order to the lattice during demagnetization was uncovered<sup>20</sup>.

In a typical femto-magnetism experiment, an intense laser pulse is irradiated onto a magnetic material such as a ferromagnet, which initiates demagnetization dynamics, spin transfer dynamics, or spin switching<sup>21–30</sup>. The ultrafast dynamics are subsequently tracked through time-resolved pump-probe spectroscopy<sup>31–34</sup>. Recently it was shown that magnetization can even be transiently induced in nonmagnetic materials with resonant circularly polarized light through the inverse Faraday effect<sup>35</sup>, which is a perturbative nonlinear optical effect<sup>36,37</sup>, or through slower spin-phonon couplings<sup>38</sup>. However, to our knowledge all experiments and theoretical works thus far have never observed or predicted the following: (i) an effect whereby a nonmagnetic material is illuminated by an intense nonresonant laser pulse that initiates a

few femtosecond turn-on of magnetization. (ii) Magnetization dynamics driven in nonmagnetic materials by linearly polarized light. (iii) Magnetization dynamics that occurs on sub-femtosecond timescales. All of these effects could pave the way to new regimes in ultrafast and non-equilibrium magnetism, e.g., allowing extremely fast manipulation of magnetic orders even in materials that have a nonmagnetic ground state.

In parallel to advancements in femto-magnetism, strong-field physics in solids has developed as an approach for controlling electron motion on sub-femtosecond timescales<sup>39–45</sup>. Strong-field interactions in solids enabled tailoring valley pseudo-spin occupations<sup>46,47</sup>, controlling material topological properties<sup>46</sup>, steering Dirac electrons<sup>48</sup> and more<sup>49–52</sup>. This regime provides an ideal setting for exploring possibilities of attosecond magnetism, because it gives natural access to attosecond electron motion (whereby electrons act as spin carriers). To capitalize this, a strong spin-orbit interaction could allow converting electronic angular momenta into magnetism (whereas light does not directly couple to spin degrees of freedom). Extremely nonlinear light-matter interactions such as high harmonic generation (HHG) have been explored in some material systems with strong spin-orbit interactions (e.g., in BiSbTeSe<sub>2</sub><sup>53</sup>, Bi<sub>2</sub>Te<sub>3</sub><sup>54</sup>, Bi<sub>2</sub>Se<sub>3</sub><sup>55</sup>, Ca<sub>2</sub>RuO<sub>4</sub><sup>56</sup>, Na<sub>3</sub>Bi<sup>57</sup>), but the induced magnetization was not investigated.

Here, we report on femto-magnetic phenomena that are driven in nonmagnetic materials by intense ultrashort laser pulses in the strong-field and highly nonlinear regime of light-matter interactions. We demonstrate with state-of-the-art time-dependent spin density functional theory calculations that strong magnetization of  $\sim 0.1 \mu_B$  (where  $\mu_B$  is a Bohr magneton) can be turned-on extremely fast when driven by nonresonant circularly polarized light, within  $\sim 16$  femtoseconds. This transient magnetic state is expected to live for several tens of femtoseconds before it is destroyed by

<sup>1</sup>Max Planck Institute for the Structure and Dynamics of Matter and Center for Free-Electron Laser Science, Hamburg 22761, Germany. <sup>2</sup>Università degli Studi di Palermo, Dipartimento di Fisica e Chimica—Emilio Segrè, Palermo I-90123, Italy. <sup>3</sup>Center for Computational Quantum Physics (CCQ), The Flatiron Institute, New York, NY 10010, USA.

✉email: ofer.neufeld@gmail.com; angel.rubio@mpsd.mpg.de

scattering and dephasing. We thoroughly analyze this effect and show that the magnetization arises from highly nonlinear multi-photon processes, which together with spin-orbit interactions, allow for attosecond spin polarization to build up over time. We also study systems irradiated by linearly polarized pulses, whereby one intuitively does not expect a magnetic response (because there is no angular momentum in the driving pulses). Remarkably, we show that even linearly polarized pulses, when sufficiently intense, can induce magnetization dynamics, owing to an interplay of electronic currents driven along the laser polarization axis and transverse anomalous currents that arise in some material systems (e.g., from a nonzero Berry curvature or other structural asymmetries). Together, these currents give rise to a sub-cycle electronic orbital angular momentum that is converted to transient attosecond magnetism. The spin expectation values can flip sign from a maximum of  $+0.01 \mu_B$  to a minimum of  $-0.01 \mu_B$  in just  $\sim 411$  attoseconds. Strikingly, the speed of magnetism can be tuned by changing the laser parameters. We outline and simulate a circular dichroism attosecond transient absorption spectroscopy setup that is capable of measuring these phenomena.

## RESULTS

### Methodology

We begin by outlining our methodological approach. To model light-induced magnetization dynamics, we employ ab initio calculations based on time-dependent spin density functional theory (TDSDF) in the Kohn–Sham (KS) formulation<sup>58</sup>. The system's ground state is directly obtained within spin-polarized DFT, and is then propagated in real-time with the following equations of motion (we use atomic units unless stated otherwise):

$$i\partial_t |\psi_{n,\mathbf{k}}^{KS}(t)\rangle = \left( \frac{1}{2} \left( -i\nabla + \frac{\mathbf{A}(t)}{c} \right)^2 \sigma_0 + v_{KS}(t) \right) |\psi_{n,\mathbf{k}}^{KS}(t)\rangle \quad (1)$$

where  $|\psi_{n,\mathbf{k}}^{KS}(t)\rangle$  is the KS–Bloch state at  $k$ -point  $\mathbf{k}$  and band index  $n$ , which is a Pauli spinor:

$$|\psi_{n,\mathbf{k}}^{KS}(t)\rangle = \begin{bmatrix} |\varphi_{n,\mathbf{k},1}^{KS}(t)\rangle \\ |\varphi_{n,\mathbf{k},2}^{KS}(t)\rangle \end{bmatrix} \quad (2)$$

with  $|\varphi_{n,\mathbf{k},a}^{KS}(t)\rangle$  the spin-up/spin-down part of the KS states with spin index  $a$ .  $\sigma_0$  in Eq. (1) is a  $2 \times 2$  identity matrix, and  $\mathbf{A}(t)$  is the vector potential of the impinging laser pulse within the dipole approximation such that  $-\partial_t \mathbf{A}(t) = c\mathbf{E}(t)$ , and  $c$  is the speed of light (in atomic units  $c \approx 137.036$ ).  $v_{KS}(t)$  is the time-dependent KS potential given by:

$$v_{KS}(t) = \int d^3r' \frac{n(\mathbf{r}',t)}{|\mathbf{r}-\mathbf{r}'|} \sigma_0 + v_{XC}[\rho(\mathbf{r},t)] + V_{ion} \quad (3)$$

where the first term in Eq. (3) is the classical Hartree term—an electrostatic mean-field interaction between electrons, where  $n(\mathbf{r},t) = \sum_{n,\mathbf{k},a} w_{\mathbf{k}} |\langle \mathbf{r} | \varphi_{n,\mathbf{k},a}^{KS}(t) \rangle|^2$  is the time-dependent electron density, with  $w_{\mathbf{k}}$  the  $k$ -point weights and the sum running over occupied bands. The second term in brackets,  $v_{XC}$ , is the exchange–correlation (XC) potential that in the local spin density approximation is a function of the spin density matrix:

$$\rho(\mathbf{r},t) = \frac{1}{2} n(\mathbf{r},t) \sigma_0 + \frac{1}{2} \mathbf{m}(\mathbf{r},t) \cdot \boldsymbol{\sigma} \quad (4)$$

where  $\mathbf{m}(\mathbf{r},t)$  is the time-dependent magnetization vector:

$$\mathbf{m}(\mathbf{r},t) = \sum_{n,\mathbf{k}} w_{\mathbf{k}} \langle \psi_{n,\mathbf{k}}^{KS}(t) | \mathbf{r} | \boldsymbol{\sigma} | \mathbf{r} | \psi_{n,\mathbf{k}}^{KS}(t) \rangle \quad (5)$$

$V_{ion}$  in Eq. (3) represents the interactions of electrons with the lattice ions and core electrons. To reduce numerical costs we

employ the frozen core approximation, and the bare Coulomb interaction between electrons and ions is replaced with a fully relativistic nonlocal norm-conserving pseudopotential<sup>59</sup>. This term also includes the full ab initio description of relativistic corrections to the Hamiltonian, including the mass term and the Darwin term. Most importantly, it incorporates a spin–orbit coupling term that is proportional to  $\mathbf{L} \cdot \mathbf{S}$ , where  $\mathbf{L} = (L_x, L_y, L_z)$  is the angular momentum operator vector, and  $\mathbf{S} = \frac{1}{2} \boldsymbol{\sigma} = \frac{1}{2} (\sigma_x, \sigma_y, \sigma_z)$  is spin operator vector, with  $\sigma_i$  the  $i$ th Pauli matrix. It is noteworthy that  $v_{KS}$  is nondiagonal in spin space due to the spin–orbit coupling term.

The interactions of electrons with the laser are described in the velocity gauge, where we employ the following vector potential:

$$\mathbf{A}(t) = f(t) \frac{cE_0}{\omega} \sin(\omega t) \hat{\mathbf{e}} \quad (6)$$

where  $f(t)$  is an envelope function (see “Methods” for details),  $E_0$  is the field amplitude,  $\omega$  is the carrier frequency, and  $\hat{\mathbf{e}}$  is a unit vector that is generally elliptically polarized. Note that we neglect ion motion and assume the frozen nuclei approximation (i.e., omitting phononic excitations). This is expected to be a very good approximation in attosecond to femtosecond timescales, especially for heavy atoms. We further emphasize that in the dipole approximation interactions with the magnetic part of the laser pulse are neglected, which might also induce magnetic responses. Such contributions are expected to be negligible in our driving conditions (laser powers  $\sim 10^{12}$  W cm<sup>-2</sup>, and wavelengths  $\sim 3000$  nm)<sup>60,61</sup>.

The KS equations of motion are solved in a real-space grid representation with Octopus code<sup>62–64</sup>. From the time-propagated KS states, we calculate time-dependent observables of interest, including the total electronic current,  $\mathbf{J}(t) = \frac{1}{\Omega} \int_{\Omega} d^3r \mathbf{j}(\mathbf{r},t)$ , where  $\Omega$  is unit cell volume and  $\mathbf{j}(\mathbf{r},t)$  is the microscopic time-dependent current density:

$$\mathbf{j}(\mathbf{r},t) = \sum_{n,\mathbf{k},a} \left[ \varphi_{n,\mathbf{k},a}^{KS*}(\mathbf{r},t) \left( \frac{1}{2} \left( -i\nabla + \frac{\mathbf{A}(t)}{c} \right) + [V_{ion}, \mathbf{r}] \right) \varphi_{n,\mathbf{k},a}^{KS}(\mathbf{r},t) \right] + \mathbf{j}_m(\mathbf{r},t), \quad (7)$$

where  $\mathbf{j}_m(\mathbf{r},t)$  is the magnetization current density (which after spatial integration vanishes and does not contribute to  $\mathbf{J}(t)$ ).  $\mathbf{J}(t)$  is also used to obtain the HHG spectra,  $\mathbf{I}(\Omega) = |\int \partial_t \mathbf{J}(t) e^{-i\omega t} dt|^2$ . The spin expectation values are calculated as  $\langle \mathbf{S}(t) \rangle = \langle \psi_{n,\mathbf{k}}^{KS}(t) | \mathbf{S} | \psi_{n,\mathbf{k}}^{KS}(t) \rangle$ , and are used to track the spin dynamics in the system. The resulting induced magnetization is given as  $\langle S_z(t) \rangle$  in units of Bohr magneton, and is summed over all atoms and occupied electronic states for a given unit cell. We refer to a nonmagnetic material as a material with strictly  $\langle \mathbf{S}(t=0) \rangle = 0$ , and where the spin expectation values vanish even when projecting on individual atomic sites in the unit cell. All other technical details about the numerical procedures are delegated to the “Methods”.

This numerical approach is employed in exemplary benchmark materials for exploring light-driven magnetization dynamics. The main example used throughout the text is the two-dimensional (2D) topological insulator, bismuthumane (BiH)<sup>65</sup>. BiH is comprised of a monolayer of bismuth atoms arranged in a honeycomb lattice (see illustration in Fig. 1a). The bismuth atoms are capped by hydrogen atoms that are bonded to the bismuth  $p_z$  orbitals in a staggered configuration that preserves inversion symmetry, but breaks some of the mirror planes of the honeycomb lattice. The electronic structure of BiH is strongly affected by spin–orbit coupling (SOC)—without SOC it exhibits Dirac cones in the K and K' high-symmetry points, but SOC opens a large topological gap with nonzero Berry curvature throughout the Brillouin zone (see Fig. 1b)<sup>65</sup>. Each band is spin-degenerate, and the ground state is nonmagnetic. BiH is an ideal candidate for exploring light-driven magnetic phenomena because the bismuth ions induce a relatively large SOC, and the system is an insulator which allows

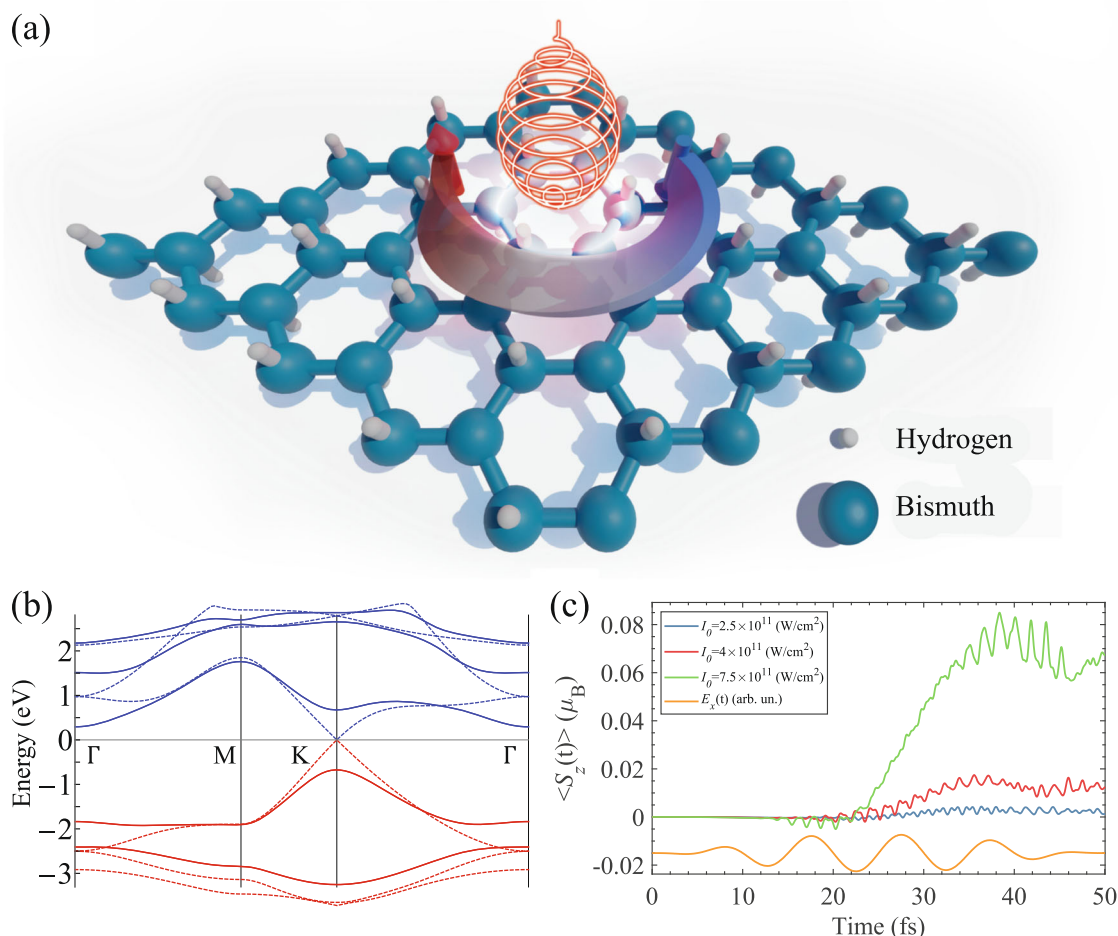


**Fig. 1 Ultrafast turn-on of magnetism in monolayer BiH.** **a** Illustration of the hexagonal BiH lattice and ultrafast turn-on of magnetism—an intense femtosecond laser pulse is irradiated onto the material, exciting electronic currents that through spin–orbit interactions induce magnetization and spin flipping. **b** Band structure of BiH with and w/o SOC (red and blue bands indicate occupied and unoccupied states, respectively). In the SOC case, each band is spin-degenerate. **c** Calculated spin expectation value,  $\langle S_z(t) \rangle$ , driven by circularly polarized pulses for several driving intensities (for a wavelength of 3000 nm). The x-component of the driving field is illustrated in arbitrary units to convey the different timescales in the dynamics.

strong nonresonant nonlinear responses (the direct gap is 1.35 eV within the local spin density approximation). As we will show below, all of our results are independent of the topological insulator character of BiH.

### Sub-cycle turn-on of magnetization

We calculate the electronic response of BiH to intense circularly polarized laser pulses (polarized in the monolayer  $xy$  plane) with a carrier wavelength of 3000 nm, and intensities in the ranges of  $10^{11}$ – $10^{12}$   $\text{W cm}^{-2}$  (see illustration in Fig. 1a). The corresponding carrier photon energy of 0.41 eV is well below the band gap, guaranteeing that the dominant light–matter response is nonresonant (at least four photons are required to excite an electron from the valence to the conduction band). These conditions result in HHG with harmonics up to the  $\sim 30$ th order corresponding to photon energies of  $\sim 12$  eV being emitted (see Supplementary Fig. 1). The circularly polarized drive imparts angular momenta onto the electronic system through the light–matter coupling term, and a combination of intraband acceleration and interband recollisions lead to the HHG emission<sup>43,66</sup>. In practical terms, the laser drive provides a means to break time-reversal symmetry in the dynamical evolution of the system—the quantum propagator does not commute with the time-reversal operator allowing for spin

degeneracies to be lifted. It is noteworthy that due to a six-fold improper-rotational symmetry in BiH, only harmonic orders of  $6n \pm 1$  are emitted for integer  $n$ , which follows from dynamical symmetry selection rules<sup>67</sup>. As we will later show, similar selection rules can be derived for the total electronic excitation and the spin expectation values, which play a significant role in the magnetization dynamics.

The interesting question that we now explore is whether the laser-driven electronic angular momenta can be converted to a net magnetization. While such conversion was recently shown in resonant conditions<sup>35</sup>, it is not clear if it can be obtained non-resonantly. Moreover, it is unknown whether this can be achieved in a system with fully spin-degenerate bands (precluding spin-selectivity via optical transitions between spin-split bands). Figure 1c shows the time-dependent expectation value of spin along the  $z$  axis,  $\langle S_z(t) \rangle$ , for several laser intensities. The BiH system is initially in a nonmagnetic ground state with  $\langle \mathbf{S}(t=0) \rangle = 0$ , but shows an onset of magnetization about 12 femtoseconds after it starts interacting with the laser. The characteristics of the magnetic response can be described by two main features: (i) sub-cycle fast oscillations of the spins, and (ii), a slower buildup of the magnetization that occurs over several laser cycles. By calculating the total occupation of electrons in just the up or down part of the spinors we verify that the induced magnetization indeed results from spin-flipping processes (see Supplementary Fig. 2). In other

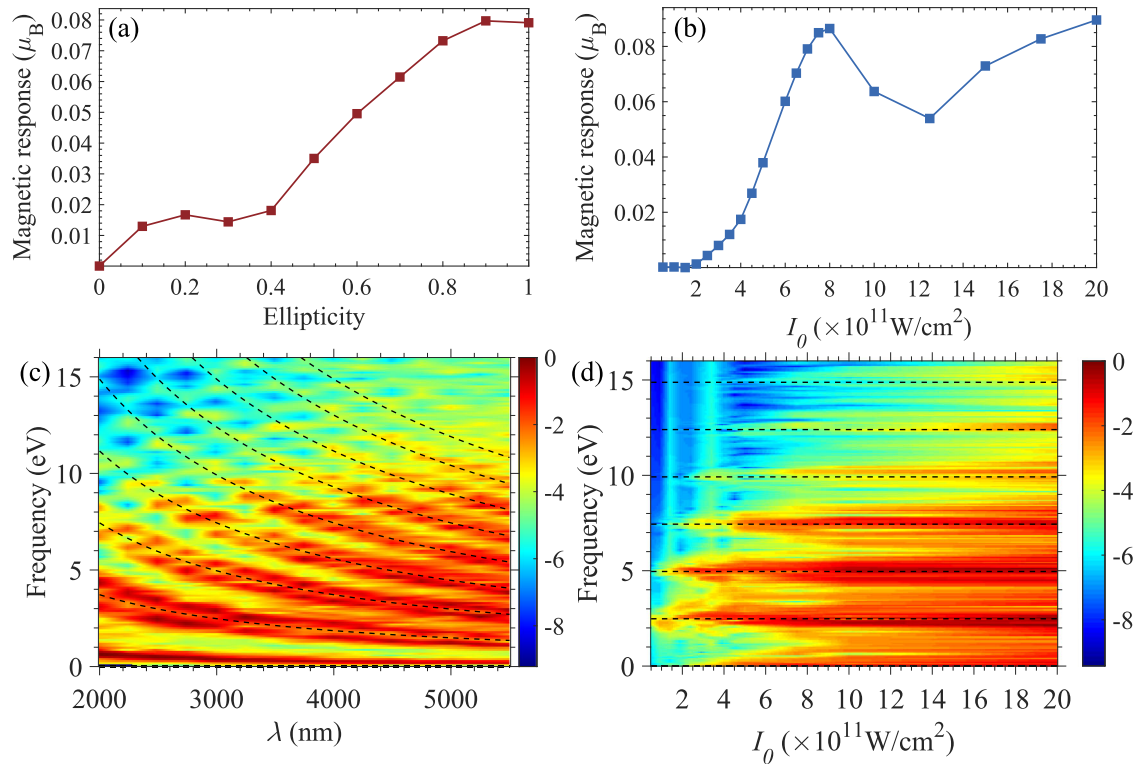


**Fig. 2** Induced magnetic response for elliptical driving in BiH for changing laser parameters. **a** Maximal induced magnetization vs. the driving laser ellipticity, for driving power of  $7 \times 10^{11} \text{ W cm}^{-2}$  and wavelength of 3000 nm, where the elliptical major axis is transverse to the Bi–Bi bonds. **b** Same as (a) but for circularly polarized driving vs. laser power. **c** Spectral components of  $\langle S_z(t) \rangle$  vs. driving wavelength (calculated for an intensity of  $5 \times 10^{11} \text{ W cm}^{-2}$ , presented in log scale). Dashed black lines indicate  $6n$  harmonics of the driving laser carrier frequency (for integer  $n$ ), showing that the spin’s temporal evolution is driven by the laser, and that its symmetries are connected to the light-driven electronic excitations. **d** Same as (c) but for changing laser intensity (for a driving wavelength of 3000 nm). Higher intensities and longer wavelengths are shown to lead to higher frequency components, indicating a faster magnetic response.

words, during the interaction with the laser spin-down electrons are flipped into a spin-up state. By reversing the helicity of the driving laser, one obtains the opposite picture with a conversion of up-to-down spins. We note that these transitions cannot occur from a resonant optical transition because the photon energies are well below the gap.

The very fast oscillations observed in Fig. 1c indicate that there are attosecond magnetization dynamics involved. For circularly polarized driving these attosecond spin-flipping processes accumulate over the laser cycle on a timescale of about ten femtoseconds, yielding a net magnetization (i.e., a long-range magnetic order). Notably, the response strongly depends on the driving power. Figure 1c shows that for stronger driving a larger net magnetization can be obtained (as high as  $\sim 0.1\mu_B$ ). This result hints to the active mechanism at play: stronger driving increases the angular momentum of the excited electrons, which increases the contribution of the SOC term. This is also supported by calculations that show that the induced magnetic response diminishes with the driving ellipticity (see Fig. 2a). The process is thus analogous to the inverse Faraday effect, but in nonresonant and nonperturbative conditions. Figure 2b presents the scaling of the magnetic response with intensity—for weaker driving, it follows a quartic dependence with the field amplitude, indicating a 4-photon response (the minimal number of photons required to excite an electron from the valence to the conduction band in these conditions), but above  $\sim 4 \times 10^{11} \text{ W cm}^{-2}$  this dependence breaks down and behaves non-perturbatively. Interestingly, we note that the induced magnetization saturates for ellipticities between 0.2 and 0.4, i.e., the magnetic response stops increasing with ellipticity for that parameter range (Fig. 2a). This behavior

differs from that of the inverse Faraday effect and reflects the extreme nonlinearity of the magnetization.

The onset time for the magnetization also strongly depends on the driving power and shows a nonperturbative nonlinear dependence (see Supplementary Fig. 3). Overall, this suggests that the spin-flipping processes are directly driven by the electronic excitations to the conduction band (because these are initiated by tunneling), which subsequently undergo additional laser-induced acceleration in the bands that lead to spin-flipping. We further support this picture with a  $k$ -space and band-resolved projection of the magnetization density, which validates that the regions around the K and K’ points (minimal band gap positions) are the dominant contributors to the induced magnetization, and that the first valence and conduction bands have the largest contribution (see Supplementary Fig. 5). We highlight that these observed dynamics differ from previously reported results in the perturbative resonant regime—the nonresonant driving here does not directly excite a spin-selective optical transition, and spin-split bands do not play any role.

Next, we analyze the electronic excitations that allow for these spin-flipping processes. Figure 2c, d plots the spectral components of the net magnetization of the system, i.e., the Fourier transform of  $\langle S_z(t) \rangle$ , vs. the driving intensity and wavelength. The main observation from Fig. 2c, d is that the spin excitation is inherently connected to the laser drive—remarkably, its spectral components are comprised of harmonics of the laser carrier frequency, and only  $6n$  harmonics (for integer  $n$ ) are allowed in the circularly polarized driving case. Supplementary Fig. 1 presents results for elliptical driving which also support this conclusion, but where  $2n$  (even) harmonics are allowed. This result is important for several reasons: (i) it directly proves that the laser-driven electron

dynamics are converted to magnetization (via SOC), because otherwise the spin would not evolve in temporal harmonics of the laser. (ii) It allows to tune the temporal behavior of the spin-flipping by changing the driving parameters. (iii) It establishes the main microscopic mechanism for the ultrafast spin-flipping processes, which involves attosecond sub-cycle excitations of electrons from the valence to the conduction band. The excited electrons are subsequently driven by the laser field that imparts angular momentum, which is converted by the SOC term to spin-flipping torques. In Supplementary Figs. 3 and 4, we show that the total number of electrons excited to the conduction band over time evolves with the same exact symmetries as the spectral components of the magnetization (e.g., six-fold in the circularly polarized driving case), and also derive the origin of this effect. Moreover, we confirm that the onset time for the magnetization dynamics is inherently connected to the electronic excitation. Thus, the two processes of strong-field tunneling between the bands, and spin flipping, are interlinked.

Notably, this mechanism follows the first steps in the HHG process in solids (i.e., tunneling of electrons to the conduction band, and subsequent acceleration in the bands)<sup>43,66</sup>, but where spin and SOC play the additional role in driving a magnetic response. Overall, the onset of ultrafast magnetization is enabled by the fact that in the strong-field regime, electrons acquire relatively large momenta (i.e., large  $\langle \mathbf{L} \rangle$ ), and that this happens repeatedly every laser cycle. The fact that electrons are driven in an extremely nonlinear manner that is inherently sensitive to attosecond sub-cycle timescales allows possibilities of atto-magnetism. Indeed, Fig. 2 shows that the electron's spin can oscillate with frequencies as high as the 42nd harmonic of the laser, which promises incredible potential for atto-magnetism (that corresponds to  $\sim 100$  attosecond magnetization dynamics, provided that the lower orders of the response can be suppressed). In Supplementary Fig. 6, we validate that the induced magnetism is not driven by electronic correlations, which tend to slightly reduce the magnitude of the phenomena (as expected due to enhanced scattering). We note that since our simulations do not include sufficient dephasing and relaxation channels (because of the use of semi-local approximations to the XC functional, and because we do not incorporate electron-phonon couplings in the simulation), the electronic and spin excitations do not fully decay in our calculations. In realistic experimental conditions, we expect that these magnetic states will live for several tens of femtoseconds before decohering.

### Attosecond magnetism

We now further analyze the very fast oscillations of magnetization seen in Fig. 1c. For circularly polarized driving, they are overlaid

on top of the dominant slow response that builds up the net magnetization from cycle to cycle. That is, the dominant spin response is a zeroth-order multipole. Consequently, it is very difficult to measure these fast oscillations experimentally or to utilize them for applications. Still, the high-energy spectral components in  $\langle \mathbf{S}(t) \rangle$  appear to be quite dominant compared to the weaker perturbative response, as long as there is a way to suppress the zeroth-order slow contribution (see, for instance, Fig. 2d).

In order to try and extract this response, we now explore linearly polarized driving, where the in-plane polarization axis is given by the angle  $\theta$ , which is the offset angle from the  $x$  axis (that is transverse to the Bi–Bi bonds). Importantly, in this case the cycle-averaged total angular momentum of the laser-matter system remains zero. In this respect, one expects no net magnetization to evolve, such that the zeroth-order multipole of  $\langle \mathbf{S}(t) \rangle$  should vanish. At the same time, intuition would dictate that no magnetization dynamics should occur at all, since even if one considers timescales shorter than a laser cycle the driving field is linearly polarized and does not contain angular momenta. Nevertheless, Fig. 3a presents the temporal evolution of  $\langle S_z(t) \rangle$  for several driving intensities, which shows a strong magnetic response that rapidly oscillates in time (on attosecond timescales). What is the origin of this transient magnetism?

Figure 3b presents the spectral components of the spin evolution vs. the in-plane laser polarization angle, which enables us to pinpoint the source of the effect. Clearly, the response follows fundamental symmetries of the material system—when the laser is polarized along a plane of BiH that exhibits a mirror or a two-fold rotational symmetry the magnetic response fully vanishes. At this stage we recall that for these driving conditions, electrons are accelerated in the bands, which generates high harmonics and nonlinear currents in the system. The hexagonal lattice of BiH drives a transverse electric current<sup>44,66,68–70</sup>. However, from fundamental symmetries these transverse currents must vanish along the same high-symmetry axes<sup>67</sup>. Figure 3c presents the HHG spectral components that are polarized only transversely to the main driving axis vs. the in-plane driving angle, which verifies this result. Notably, the emitted HHG radiation polarized transverse to the driving axis, and the spectral components of the magnetic response, are extremely similar (compare Fig. 3b, c). We thus conclude that a transverse current component is essential for generating the magnetic response. In accordance with the mechanism described above, this result is clear—the electronic system must acquire a nonzero angular momentum,  $\langle \mathbf{L} \rangle$ , since only then the SOC term can initiate a net magnetism (given that the system starts out in a nonmagnetic state). Such angular momenta is only obtained if electrons are

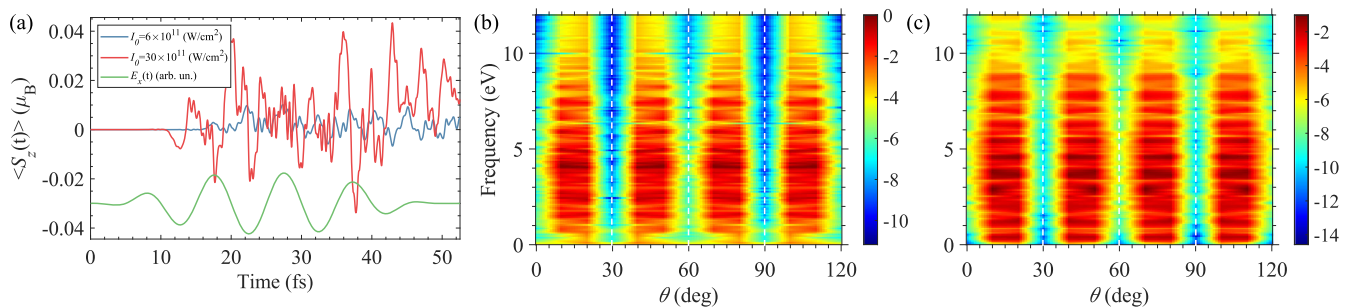


**Fig. 3 Attosecond light-driven magnetic response in BiH.** **a** Exemplary calculations of  $\langle S_z(t) \rangle$  driven by intense linearly polarized pulses for several driving intensities (for a driving wavelength of 3000 nm and a polarization angle of  $\theta = 10^\circ$ ), showing attosecond timescale magnetization dynamics. The driving field is illustrated in arbitrary units to convey the different timescales in the dynamics. **b** Spectral components of  $\langle S_z(t) \rangle$  vs. driving angle. The magnetic response vanishes along high-symmetry axes (indicated by white dashed lines). Plot calculated for a driving intensity of  $2 \times 10^{11} \text{ W cm}^{-2}$  and a wavelength of 3000 nm. **c** The HHG spectra polarized transversely to the driving laser axis, vs. the driving laser polarization axis in the monolayer plane. The transverse currents vanish for the same driving conditions as the magnetic response, indicating that the two are connected. **b, c** The spectral power is presented in log scale.

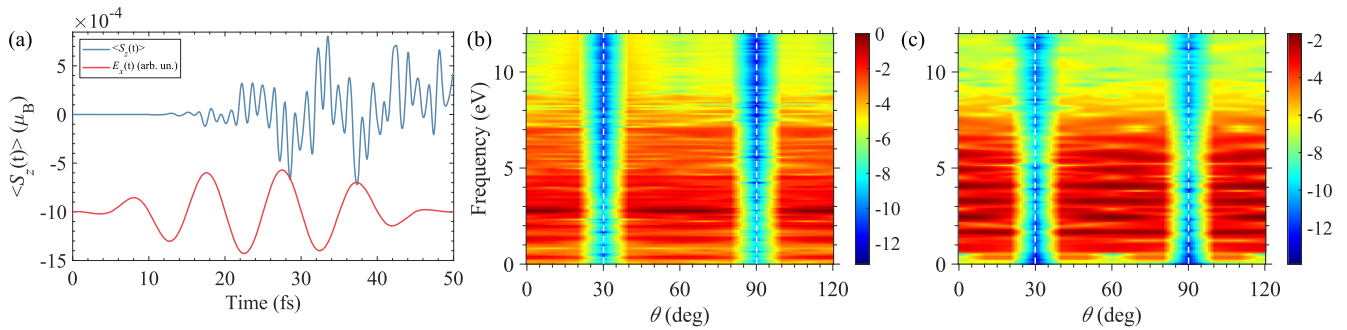


**Fig. 4 Ultrafast turn-on of magnetization and attosecond magnetization dynamics in monolayer H-MoTe<sub>2</sub> (topologically trivial).** **a** Exemplary calculation of  $\langle S_z(t) \rangle$  driven by a linearly polarized pulse with an intensity of  $2 \times 10^{11} \text{ W cm}^{-2}$ , a wavelength of 3000 nm, and polarized at  $\theta = 20^\circ$ . The driving field is illustrated in arbitrary units to convey the different timescales in the dynamics. **b** Spectral components of  $\langle S_z(t) \rangle$  vs. driving angle in the same conditions as (a). **c** The HHG spectra polarized transversely to the driving laser axis, vs. the driving laser polarization axis in the monolayer plane. **b, c** The spectral power is presented in log scale. Dashed white lines indicate high-symmetry axes.

driven in at least two transverse axes. Thus, the transverse currents in this case act as a key ingredient for the magnetic response, since they initialize transverse electron motion that mimics the effects of circularly polarized driving. Indeed, if the SOC term is turned off the magnetic response completely vanishes (see Supplementary Fig. 6). From the perspective of symmetries, the quantum propagator from the start to the end of the laser pulse approximately commutes with the time-reversal operator because the laser is linearly polarized (up to contributions from the pulse envelope). Thus again, one intuitively does not expect a magnetization to arise at all. On shorter timescales however, where consecutive half-cycles did not yet have time to cancel out each other's action, time-reversal symmetry can be transiently broken and allow a magnetic response to develop.

We stress that after the laser-matter interaction has ended, the system is left in a nonmagnetic state as expected (the magnetization along each half-cycle cancels out), removing the zeroth-order spin response. Thus, linearly polarized driving enables the higher-order spin dynamics to be uncovered, and even dominate over the slower perturbative responses. Arguably, one of the most exciting consequences is that the magnetic response oscillates very rapidly during the interaction with the laser. For instance, in an extreme case we observe the magnetization flipping from a local maximum of  $\sim 0.01\mu_B$  to a local minimum of  $\sim -0.01\mu_B$  within just 411 attoseconds (see Fig. 3a).

### Other materials

At this point one may wonder about the generality of our results, since we studied light-driven dynamics in a 2D topological insulator. Thus, a legitimate question is whether the obtained ultrafast magnetization is a topological feature, and if it is also applicable in 3D bulk solids. To address these questions we explore the ultrafast magnetic response in MoTe<sub>2</sub>, which is a transition metal dichalcogenide, and bulk Na<sub>3</sub>Bi<sup>71</sup>. Specifically, we consider the 2H bulk phase and the H monolayer phases of MoTe<sub>2</sub>, which are non-topological and have nonmagnetic ground states. Na<sub>3</sub>Bi on the other hand has a topological nature, and was recently shown to be a Dirac semimetal with bulk Dirac cones appearing at finite momenta<sup>71,72</sup>. We consider it because it is a peculiar example for a 3D material system with strong SOC, a nonmagnetic ground state, and inherently vanishing Berry curvature, but which still permits generation of transverse anomalous currents due to its hexagonal structure.

Figure 4a presents an exemplary temporal evolution of  $\langle S_z(t) \rangle$  driven by an intense linearly polarized pulse in a monolayer of H-MoTe<sub>2</sub>. Figure 4b presents the spectral components of  $\langle S_z(t) \rangle$  for linear driving vs. the in-plane driving angle. Clearly, similar ultrafast magnetic responses are obtained; albeit, they are slightly weaker because MoTe<sub>2</sub> exhibits weaker SOC (from an

experimental perspective, a choice of heavy elements with strong SOC is preferred). Thus, a main conclusion is that the attosecond-based magnetism is driven in nonmagnetic materials independently on if the bands have nonzero Chern numbers or not. In general, very similar nonlinear behavior is obtained in MoTe<sub>2</sub> for all driving conditions (see Supplementary Fig. 7). Figure 4c presents the corresponding HHG spectra polarized transverse to the laser driving. Very good agreement between the two is obtained just as was seen in BiH (regardless of the different space group of MoTe<sub>2</sub> and BiH), confirming the generality of the results outlined above. In Supplementary Fig. 8, we also present results for the bulk phase, which shows similar responses.

Similarly, in Supplementary Fig. 9, we show that for linearly polarized driving there is a strong magnetic response in Na<sub>3</sub>Bi. This is despite the fact that it has uniformly vanishing Berry curvature<sup>71</sup>, and results from the hexagonal lattice that permits nonzero transverse currents to first order of the driving field (whereas Berry curvature is typically associated with a second-order nonlinear response), as long as it is not driven along high-symmetry axes. Indeed, along mirror planes there are no transverse currents in Na<sub>3</sub>Bi, and consequently, also no light-induced magnetization dynamics. Thus, our results indicate a general mechanism that enables attosecond magnetism in otherwise nonmagnetic systems, including 3D bulk solids and 2D systems. The main ingredients for this response are: (i) highly nonresonant strong-field driving, (ii) strong spin-orbit coupling, and (iii) generation of transverse currents to the driving which are permitted by crystal symmetries, and which effectively yield a strong oscillating orbital angular momentum.

### Pump-probe circular dichroism

Lastly, we present a potential experimental setup capable of measuring these attosecond magnetic responses. This setup is based on a pump-probe geometry, where the pump is an intense femtosecond pulse that excites magnetization dynamics (just as in Eq. (6)), and the probe is a weaker ultrashort sub-femtosecond pulse that is circularly (or elliptically) polarized (as utilized in ref. <sup>34</sup>, but with lower-energy probe pulses). By measuring the time-resolved circular dichroism (CD) in the absorption (or transmission) spectra, one can detect attosecond magnetism (for numerical details, see "Methods"). Notably, since the ground states for all of the material systems we examined are nonmagnetic, the CD is zero if the system is not pumped such that nonzero signals immediately indicate the presence of magnetization.

Figure 5a presents an exemplary spectrum for BiH driven by a circularly polarized pulse—the strong pump field induces changes to the imaginary part of the material's dielectric function. When this driven state of matter is probed with left circularly polarized (LCP) or right circularly polarized (RCP) pulses, there is a noticeable

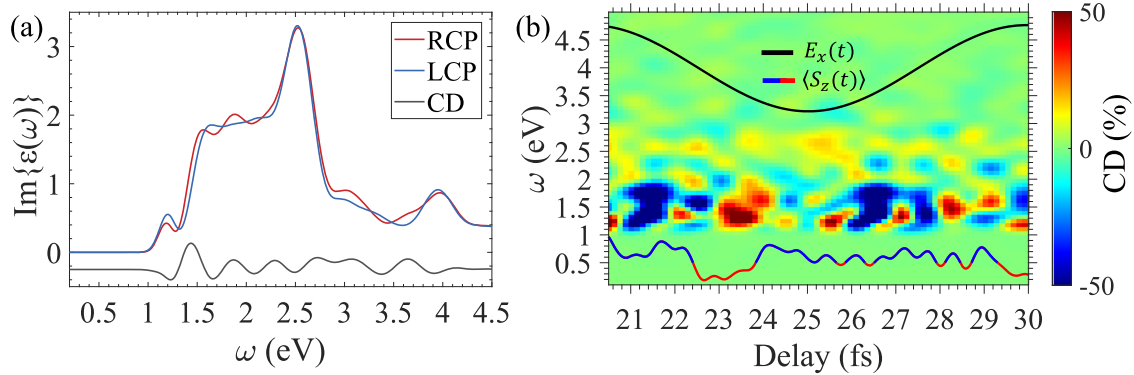


**Fig. 5 Pump-probe time-resolved CD absorption spectroscopy in BiH.** **a** Imaginary part of the dielectric function for the driven system (pumped with a circularly polarized pulse with a wavelength of 3000 nm and intensity  $7.5 \times 10^{11} \text{ W cm}^{-2}$ ), probed with either left (LCP) or right (RCP) helical probes. The driven system is temporally probed one cycle before the end of the pump laser field. The CD curve represents the subtraction between the RCP and LCP curves and is shifted down for clarity. Note that due to its finite duration, the probe pulse has a non-uniform ellipticity in this frequency region, which is not taken into account in **(a)**. **b** Attosecond-resolved CD in the linear driving case (for a wavelength of 3000 nm and intensity  $3 \times 10^{12} \text{ W cm}^{-2}$ , driven at an angle of  $\theta = 20^\circ$ ). The  $x$ -component of the driving electric field and the induced magnetization is plotted out of scale for reference in black (top), where positive/negative parts of the induced magnetization are highlighted by blue/red colors (bottom) in correspondence with the CD. The CD in **(b)** is normalized by the ellipticity of the probe pulse for each frequency region.

deviation in the response. The subtraction defines the CD, which can be further normalized to the ellipticity of the probe pulse in a given spectral region (because the probe pulse has a finite duration, it is not perfectly circular and has an ellipticity of about 0.5 in the spectral region of interest). Depending on the conditions, the ellipticity-normalized CD can reach up to 50% changes of the dielectric function in equilibrium, which should be well within experimental detectability. Figure 5b presents the attosecond-resolved CD for the linearly-driven case. A strong CD signal oscillates rapidly in qualitative agreement with the induced magnetization (peak to minima changes occur on a timescale of  $\sim 500$  attoseconds), illustrating that the attosecond magnetization dynamics should be experimentally accessible. We also note that one does not generally expect a perfect correspondence between the temporally resolved CD, and the total magnetization. This is because some CD can also arise from other sources such as light-driven asymmetry in the band occupations, and because the magnetization dynamics are not energetically resolved. Still, the two correspond quite well in Fig. 5b with similar timescales for oscillations, and regions of sign changes, indicating that the majority of the CD originates from transient magnetism. We also highlight that while this particular experimental setup is quite challenging (e.g., requiring half-cycle duration laser pulses with a carrier frequency of few eV), favorable conditions should appear in materials with larger band gaps (permitting using higher energy carrier waves), as well as in bulk phases (which should increase the signal-to-noise ratio).

## DISCUSSION

To summarize, we investigated light-matter interactions between intense nonresonant femtosecond laser pulses and solids with strong spin-orbit coupling. Through state-of-the-art ab initio calculations, we demonstrated that the attosecond timescale excitation and acceleration of electrons in the bands (which involves highly nonlinear multi-photon processes) is converted to magnetism by the SOC term. With circularly polarized driving, this induces a net magnetization that typically turns on within  $\sim 16$  femtoseconds. Consequently, we establish a regime of femto-magnetism where nonmagnetic materials can be transiently transformed into long-range ordered magnetic states with nonresonant driving. Remarkably, even in linearly polarized driving conditions there are significant magnetization dynamics during the interaction with the laser pulse, which are enabled by

light-driven anomalous currents in materials that permit a transverse optical response. These dynamics evolve intrinsically on very ultrafast timescales (much faster than previously described) of  $\sim 500$  attoseconds, as they result from the extreme nonlinear response of electrons to the driving lightwave itself, on a sub-cycle level. We studied the connection between the symmetries of the laser-matter system and the induced nonlinear magnetic response, showing that the magnetization evolves in higher harmonics of the laser (up to the 42nd harmonic that oscillates at  $\sim 100$  attoseconds), and that the speed of the magnetization dynamics can be tuned with the laser parameters. To our knowledge, these are the fastest known magnetization dynamics in solids, which are enabled by the extreme nonlinearity in the strong-field regime, and the linearly polarized drive that effectively removes slower terms in the magnetic response. They should pave the way towards attosecond control of magnetism, and motivate utilizing strong-field physics as an avenue for nonlinear spintronics with enhanced degrees of control over higher-order spin and spin-photon interactions. Lastly, we showed that these phenomena should be experimentally detectable with pump-probe attosecond transient absorption experiments, utilizing circular dichroism<sup>34,73–75</sup>.

It is worth discussing some possible applications and extensions of our results. First, while we employed here simple quasi-monochromatic laser pulses, our results are more general. In that respect, utilizing more complex waveforms such as bi-chromatic fields should enable enhanced control over magnetism. This simply follows from the enhanced control over electron dynamics that such fields offer<sup>46,76,77</sup>. This possibility is especially exciting because it could lead to even further increase of the speed of the magnetization dynamics, and to controlling ultrafast magnetization by tuning the laser phases (i.e., a form of coherent control). Second, by using few-cycle pulses, we expect that one could induce a net magnetization even with linearly polarized pulses, since then transverse current contributions from sequential half-cycles would not cancel out. This would establish a magnetic analog to transient injection currents that have recently been measured<sup>41,50,51</sup>. Lastly, since the magnetization is driven in the same conditions that allow for high harmonic generation, it could enable high harmonic spectroscopy for probing magnetism, which has not been possible before<sup>57</sup>. These extensions could also offer means for further enhancing the magnitude of the induced magnetization. Looking forward, we expect our results to motivate more experimental and theoretical work in the field.

## METHODS

### Ground-state calculations

We report here on technical details for calculations presented in the main text. We start with details of the ground state DFT calculations that were used for obtaining the initial KS states. All DFT calculations were performed using Octopus code<sup>62–64</sup>. The KS equations were discretized on a Cartesian grid with the shape of the primitive lattice cells. Atomic geometries and lattice parameters were taken from ref. <sup>65</sup> for BiH ( $a = b = 5.53 \text{ \AA}$ , and a Bi–H distance of  $1.82 \text{ \AA}$ ), taken as  $a = b = 3.55 \text{ \AA}$  for H-MoTe<sub>2</sub>, as  $a = b = 3.56 \text{ \AA}$ ,  $c = 15.35 \text{ \AA}$  for 2H-MoTe<sub>2</sub>, and as  $a = b = 5.448 \text{ \AA}$ ,  $c = 9.655 \text{ \AA}$  for Na<sub>3</sub>Bi<sup>71</sup>. In all cases, the space-group symmetric primitive unit cell was employed (with the hexagonal lattice vectors residing in the  $xy$  plane). For monolayer systems, the  $z$  axis (transverse to the monolayer) was described using non-periodic boundaries with a length of 60 Bohr. The KS equations were solved to self-consistency with a tolerance  $< 10^{-7}$  Hartree, and the grid spacing used was 0.39 Bohr for BiH, and 0.36 Bohr for MoTe<sub>2</sub> and Na<sub>3</sub>Bi. We employed a  $\Gamma$ -centered  $24 \times 24 \times 1$   $k$ -grid for BiH, of  $30 \times 30 \times 1$   $k$ -grid for H-MoTe<sub>2</sub>,  $24 \times 24 \times 8$   $k$ -grid for 2H-MoTe<sub>2</sub>, and  $28 \times 28 \times 15$   $k$ -grid for Na<sub>3</sub>Bi. Deep core states were replaced by Hartwigsen–Goedecker–Hutter (HGH) norm-conserving pseudopotentials<sup>59</sup>.

### Time-dependent calculations

For the time propagation of the main equations of motion we employed a time-step of 4.83 attoseconds. The propagator was represented by a Lanczos expansion and  $k$ -point symmetries were not assumed. In the time-dependent calculations of the monolayer systems, we employed absorbing boundaries through complex absorbing potentials (CAPs) along the aperiodic  $z$  axis with a width of 15 Bohr<sup>78</sup> and a magnitude of 1 a.u. We calculated the total electronic excitation induced in the system in a time-resolved manner ( $n_{ex}(t)$ ) by projecting the KS–Bloch states onto the ground state system:

$$n_{ex}(t) = N_e - \sum_{n, n' \in VB} \sum_{\mathbf{k} \in BZ} w_{\mathbf{k}} \left| \langle \psi_{n', \mathbf{k}}^{KS}(t=0) | \psi_{n, \mathbf{k}}^{KS}(t) \rangle \right|^2 \quad (8)$$

where  $N_e$  is the total number of active electrons in the unit cell, the projections are performed onto the valence bands of the ground state system (i.e.,  $n' \in VB$ ), and the summation is performed in the entire first Brillouin zone (BZ).  $n_{ex}(t)$  gives a measure for the number of excited electrons during the light-driven dynamics.

The envelope function of the employed laser pulse,  $f(t)$  from Eq. (1), was taken to be of the following “super-sine” form<sup>79</sup>:

$$f(t) = \left( \sin \left( \pi \frac{t}{T_p} \right) \right) \left( \frac{\pi \left( \frac{t}{T_p} - \frac{1}{2} \right)}{w} \right) \quad (9)$$

where  $w = 0.75$ ,  $T_p$  is the duration of the laser pulse which was taken to be  $T_p = 5T$  ( $\sim 29.3$  femtoseconds full-width-half-max (FWHM) for 3000 nm light), where  $T$  is a single cycle of the fundamental carrier frequency. This form is roughly equivalent to a super-Gaussian pulse, but where the field starts and ends exactly at zero amplitude, which is numerically more convenient.

### Circular dichroism calculations

Calculations of transient absorption spectroscopy employed the real-time propagation approach detailed in ref. <sup>80</sup>. We employed short wide-spectrum pulses as probes that were comprised of a set of 8 stepwise jumps in the vector potential (each giving a Dirac Delta function peak in the time-domain electric field), which had a rotating polarization direction. Each step was polarized at  $45^\circ$ , and was separated by 62.9 attoseconds, with respect to its previous, resembling an optical centrifuge<sup>81</sup>. The total temporal duration of

the probe pulse is thus 503.1 attoseconds, and each peak had an intensity of  $10^{10} \text{ W cm}^{-2}$  (which gives an intensity of  $\sim 10^8 \text{ W cm}^{-2}$  in the frequency region of interest of 1–5 eV). To change the helicity of the probe pulses the direction of rotation of the centrifuge was rotated, and for normalization purposes the ellipticity of the probe was calculated using Stokes parameters<sup>82</sup> in the frequency region of interest. This configuration allows calculating the CD in a wide frequency range with attosecond temporal resolution while avoiding performing many separate calculations with changing carrier wavelength (because the step-like nature of the probe pulse has an infinite frequency content).

By calculating the light-driven current in the system, we extracted the optical conductivity via:

$$\sigma_{ij}(\omega) = \frac{\tilde{J}_{probe,i}(\omega)}{\tilde{E}_{probe,i}(\omega)} \quad (10)$$

where  $\tilde{J}_{probe,i}(\omega)$  is the Fourier transform of the total current in the system that is induced solely by the probe pulse. That is, in the time-domain  $\mathbf{J}_{probe}(t)$  is defined as the subtraction of the total current that is calculated with the presence of the probe pulse, and the current that is calculated without a probe pulse that is driven solely by the pump. Here,  $\tilde{\mathbf{E}}_{probe}$  is the Fourier transform of the electric field vector of the probe pulse, and  $i, j$  are Cartesian indices. From the optical conductivity, we extracted the dielectric function:

$$\varepsilon_{ij}(\omega) = 1 + \frac{4\pi}{\omega} \sigma_{ij}(\omega) \quad (11)$$

and the average dielectric function  $\varepsilon(\omega) = (\varepsilon_{xx}(\omega) + \varepsilon_{yy}(\omega))/2$ . The CD was calculated between the imaginary part of the dielectric functions for a right- and left-circular probe:

$$CD(\omega) = \text{Im}\{\varepsilon^+(\omega) - \varepsilon^-(\omega)\} \quad (12)$$

where  $+/-$  refers to left or right circularly polarized probes. Equation (12) was evaluated for different pump–probe delays by changing the onset time of the probe pulse, where for the temporally resolved plot in Fig. 5b we used steps of 500 attoseconds in the pump–probe delay grid and results were interpolated by splines on a denser grid. We also filtered the induced probe current,  $\mathbf{J}_{probe}(t)$ , with an exponential mask in the time domain to avoid numerical issues with the finite time propagation, and filtered  $\varepsilon_{ij}(\omega)$  with an exponential mask below the band gap to remove issues of division by zero (because the probe pulse has zero spectral components at  $\omega = 0$ ).

### DATA AVAILABILITY

All the data that supports the findings in this study is available in the main text and supplementary information file. Additional data is available upon reasonable request from the authors.

### CODE AVAILABILITY

Octopus code that was used for performing all of the simulations in the main texts is available at <http://www.octopus-code.org>.

Received: 6 September 2022; Accepted: 7 March 2023;

Published online: 23 March 2023

### REFERENCES

1. Coey, J. M. D. *Magnetism and Magnetic Materials* (Cambridge University Press, 2010).
2. Auerbach, A. *Interacting Electrons and Quantum Magnetism* (Springer Science & Business Media, 2012).
3. Yu, X. Z. et al. Real-space observation of a two-dimensional skyrmion crystal. *Nature* **465**, 901–904 (2010).
4. Seki, S., Yu, X. Z., Ishiwata, S. & Tokura, Y. Observation of skyrmions in a multi-ferroic material. *Science* **336**, 198–201 (2012).



5. Woo, S. et al. Observation of room-temperature magnetic skyrmions and their current-driven dynamics in ultrathin metallic ferromagnets. *Nat. Mater.* **15**, 501–506 (2016).
6. Das, S. et al. Observation of room-temperature polar skyrmions. *Nature* **568**, 368–372 (2019).
7. Otrokov, M. M. et al. Prediction and observation of an antiferromagnetic topological insulator. *Nature* **576**, 416–422 (2019).
8. Mishra, S. et al. Topological frustration induces unconventional magnetism in a nanographene. *Nat. Nanotechnol.* **15**, 22–28 (2020).
9. Pupal, P. et al. Topological magnetic phase in the candidate Weyl semimetal CeAlGe. *Phys. Rev. Lett.* **124**, 17202 (2020).
10. Kimel, A. V., Kirilyuk, A. & Rasing, T. Femtosecond opto-magnetism: ultrafast laser manipulation of magnetic materials. *Laser Photon. Rev.* **1**, 275–287 (2007).
11. Kirilyuk, A., Kimel, A. V. & Rasing, T. Ultrafast optical manipulation of magnetic order. *Rev. Mod. Phys.* **82**, 2731–2784 (2010).
12. Mathias, S. et al. Ultrafast element-specific magnetization dynamics of complex magnetic materials on a table-top. *J. Electron Spectrosc. Relat. Phenom.* **189**, 164–170 (2013).
13. Kalashnikova, A. M., Kimel, A. V. & Pisarev, R. V. Ultrafast opto-magnetism. *Phys.-Uspekhi* **58**, 969–980 (2015).
14. Walowski, J. & Münzenberg, M. Perspective: Ultrafast magnetism and THz spintronics. *J. Appl. Phys.* **120**, 140901 (2016).
15. Li, J., Yang, C.-J., Mondal, R., Tzschaschel, C. & Pal, S. A perspective on nonlinearities in coherent magnetization dynamics. *Appl. Phys. Lett.* **120**, 50501 (2022).
16. Koopmans, B., van Kampen, M., Kohlhepp, J. T. & de Jonge, W. J. M. Ultrafast magneto-optics in nickel: magnetism or optics? *Phys. Rev. Lett.* **85**, 844–847 (2000).
17. La-O-Vorakiat, C. et al. Ultrafast demagnetization measurements using extreme ultraviolet light: comparison of electronic and magnetic contributions. *Phys. Rev. X* **2**, 011005 (2012).
18. Rudolf, D. et al. Ultrafast magnetization enhancement in metallic multilayers driven by superdiffusive spin current. *Nat. Commun.* **3**, 1037 (2012).
19. Turgut, E. et al. Controlling the competition between optically induced ultrafast spin-flip scattering and spin transport in magnetic multilayers. *Phys. Rev. Lett.* **110**, 197201 (2013).
20. Tauchert, S. R. et al. Polarized phonons carry angular momentum in ultrafast demagnetization. *Nature* **602**, 73–77 (2022).
21. Stanciu, C. D. et al. All-optical magnetic recording with circularly polarized light. *Phys. Rev. Lett.* **99**, 47601 (2007).
22. Schellekens, A. J., Kuiper, K. C., de Wit, R. R. J. C. & Koopmans, B. Ultrafast spin-transfer torque driven by femtosecond pulsed-laser excitation. *Nat. Commun.* **5**, 4333 (2014).
23. Elliott, P., Müller, T., Dewhurst, J. K., Sharma, S. & Gross, E. K. U. Ultrafast laser induced local magnetization dynamics in Heusler compounds. *Sci. Rep.* **6**, 38911 (2016).
24. Willems, F. et al. Optical inter-site spin transfer probed by energy and spin-resolved transient absorption spectroscopy. *Nat. Commun.* **11**, 871 (2020).
25. Steil, D. et al. Efficiency of ultrafast optically induced spin transfer in Heusler compounds. *Phys. Rev. Res.* **2**, 23199 (2020).
26. Scheid, P., Sharma, S., Malinowski, G., Mangin, S. & Lebègue, S. Ab initio study of helicity-dependent light-induced demagnetization: from the optical regime to the extreme ultraviolet regime. *Nano Lett.* **21**, 1943–1947 (2021).
27. Gollas, E. et al. Ultrafast optically induced ferromagnetic state in an elemental antiferromagnet. *Phys. Rev. Lett.* **126**, 107202 (2021).
28. Hofner, M. et al. Ultrafast optically induced spin transfer in ferromagnetic alloys. *Sci. Adv.* **6**, eaay8717 (2022).
29. Phoebe, T. et al. Direct light-induced spin transfer between different elements in a spintronic Heusler material via femtosecond laser excitation. *Sci. Adv.* **6**, eaaz1100 (2022).
30. He, J., Li, S., Zhou, L. & Frauenheim, T. Ultrafast light-induced ferromagnetic state in transition metal dichalcogenides monolayers. *J. Phys. Chem. Lett.* **13**, 2765–2771 (2022).
31. Kimel, A. V., Kirilyuk, A., Tsvetkov, A., Pisarev, R. V. & Rasing, T. Laser-induced ultrafast spin reorientation in the antiferromagnet TmFeO<sub>3</sub>. *Nature* **429**, 850–853 (2004).
32. Cheng, O. H.-C., Son, D. H. & Sheldon, M. Light-induced magnetism in plasmonic gold nanoparticles. *Nat. Photonics* **14**, 365–368 (2020).
33. Zayko, S. et al. Ultrafast high-harmonic nanoscopy of magnetization dynamics. *Nat. Commun.* **12**, 6337 (2021).
34. Siegrist, F. et al. Light-wave dynamic control of magnetism. *Nature* **571**, 240–244 (2019).
35. Okyay, M. S., Kulahlioglu, A. H., Kochan, D. & Park, N. Resonant amplification of the inverse Faraday effect magnetization dynamics of time reversal symmetric insulators. *Phys. Rev. B* **102**, 104304 (2020).
36. Battiato, M., Barbalinardo, G. & Oppeneer, P. M. Quantum theory of the inverse Faraday effect. *Phys. Rev. B* **89**, 14413 (2014).
37. Scholl, C., Vollmar, S. & Schneider, H. C. Off-resonant all-optical switching dynamics in a ferromagnetic model system. *Phys. Rev. B* **99**, 224421 (2019).
38. Shin, D. et al. Phonon-driven spin-Floquet magneto-valleytronics in MoS<sub>2</sub>. *Nat. Commun.* **9**, 638 (2018).
39. Baltuška, A. et al. Attosecond control of electronic processes by intense light fields. *Nature* **421**, 611–615 (2003).
40. Goulielmakis, E. et al. Attosecond control and measurement: lightwave electronics. *Science* **317**, 769–775 (2007).
41. Schultze, M. et al. Controlling dielectrics with the electric field of light. *Nature* **493**, 75–78 (2013).
42. Ghimire, S. et al. Strong-field and attosecond physics in solids. *J. Phys. B At. Mol. Opt. Phys.* **47**, 204030 (2014).
43. Ghimire, S. & Reis, D. A. High-harmonic generation from solids. *Nat. Phys.* **15**, 10–16 (2019).
44. Uzan, A. J. et al. Attosecond spectral singularities in solid-state high-harmonic generation. *Nat. Photonics* **14**, 183–187 (2020).
45. Hui, D. et al. Attosecond electron motion control in dielectric. *Nat. Photonics* **16**, 33–37 (2022).
46. Jiménez-Galán, Á., Silva, R. E. F., Smirnova, O. & Ivanov, M. Lightwave control of topological properties in 2D materials for sub-cycle and non-resonant valley manipulation. *Nat. Photonics* **14**, 728–732 (2020).
47. Jiménez-Galán, Á., Silva, R. E. F., Smirnova, O. & Ivanov, M. Sub-cycle valleytronics: control of valley polarization using few-cycle linearly polarized pulses. *Optica* **8**, 277–280 (2021).
48. Reimann, J. et al. Subcycle observation of lightwave-driven Dirac currents in a topological surface band. *Nature* **562**, 396–400 (2018).
49. Langer, F. et al. Lightwave-driven quasiparticle collisions on a subcycle timescale. *Nature* **533**, 225–229 (2016).
50. Higuchi, T., Heide, C., Ullmann, K., Weber, H. B. & Hommelhoff, P. Light-field-driven currents in graphene. *Nature* **550**, 224–228 (2017).
51. Heide, C., Higuchi, T., Weber, H. B. & Hommelhoff, P. Coherent electron trajectory control in graphene. *Phys. Rev. Lett.* **121**, 207401 (2018).
52. Langer, F. et al. Lightwave valleytronics in a monolayer of tungsten diselenide. *Nature* **557**, 76–80 (2018).
53. Bai, Y. et al. High-harmonic generation from topological surface states. *Nat. Phys.* **17**, 311–315 (2021).
54. Schmid, C. P. et al. Tunable non-integer high-harmonic generation in a topological insulator. *Nature* **593**, 385–390 (2021).
55. Baykusheva, D. et al. All-optical probe of three-dimensional topological insulators based on high-harmonic generation by circularly polarized laser fields. *Nano Lett.* **21**, 8970–8978 (2021).
56. Uchida, K. et al. High-order harmonic generation and its unconventional scaling law in the mott-insulating Ca<sub>2</sub>RuO<sub>4</sub>. *Phys. Rev. Lett.* **128**, 127401 (2022).
57. Tancogne-Dejean, N., Eich, F. G. & Rubio, A. Effect of spin-orbit coupling on the high harmonics from the topological Dirac semimetal Na<sub>3</sub>Bi. *NPJ Comput. Mater.* **8**, 145 (2022).
58. Marques, M. A. L. & Gross, E. K. U. Time-dependent density functional theory. In: Fiolhais, C., Nogueira, F. & Marques, M. A. L. (eds) *A Primer in Density Functional Theory*. Lecture Notes in Physics, Vol 620, 144–181. (Springer, Berlin, Heidelberg, 2003). [https://doi.org/10.1007/3-540-37072-2\\_4](https://doi.org/10.1007/3-540-37072-2_4).
59. Hartwigsen, C., Goedecker, S. & Hutter, J. Relativistic separable dual-space Gaussian pseudopotentials from H to Rn. *Phys. Rev. B* **58**, 3641–3662 (1998).
60. Walsler, M. W., Keitel, C. H., Scrinzi, A. & Brabec, T. High harmonic generation beyond the electric dipole approximation. *Phys. Rev. Lett.* **85**, 5082–5085 (2000).
61. Ludwig, A. et al. Breakdown of the dipole approximation in strong-field ionization. *Phys. Rev. Lett.* **113**, 243001 (2014).
62. Castro, A. et al. octopus: a tool for the application of time-dependent density functional theory. *Phys. Status Solidi* **243**, 2465–2488 (2006).
63. Andrade, X. et al. Real-space grids and the Octopus code as tools for the development of new simulation approaches for electronic systems. *Phys. Chem. Chem. Phys.* **17**, 31371–31396 (2015).
64. Tancogne-Dejean, N. et al. Octopus, a computational framework for exploring light-driven phenomena and quantum dynamics in extended and finite systems. *J. Chem. Phys.* **152**, 124119 (2020).
65. Song, Z. et al. Quantum spin Hall insulators and quantum valley Hall insulators of BiX/SbX (X=H, F, Cl and Br) monolayers with a record bulk band gap. *NPG Asia Mater.* **6**, e147–e147 (2014).
66. Yue, L. & Gaarde, M. B. Introduction to theory of high-harmonic generation in solids: tutorial. *J. Opt. Soc. Am. B* **39**, 535–555 (2022).
67. Neufeld, O., Podolsky, D. & Cohen, O. Floquet group theory and its application to selection rules in harmonic generation. *Nat. Commun.* **10**, 405 (2019).
68. Luu, T. T. & Wörner, H. J. Measurement of Berry curvature of solids using high-harmonic spectroscopy. *Nat. Commun.* **9**, 916 (2018).

69. Silva, R. E. F., Jiménez-Galán, Á., Amorim, B., Smirnova, O. & Ivanov, M. Topological strong-field physics on sub-laser-cycle timescale. *Nat. Photonics* **13**, 849–854 (2019).
70. Baykusheva, D. et al. Strong-field physics in three-dimensional topological insulators. *Phys. Rev. A* **103**, 23101 (2021).
71. Wang, Z. et al. Dirac semimetal and topological phase transitions in  $A_3Bi$  ( $A=Na,K,Rb$ ). *Phys. Rev. B* **85**, 195320 (2012).
72. Liu, Z. K. et al. Discovery of a three-dimensional topological Dirac semimetal,  $Na_3Bi$ . *Science* **343**, 864–867 (2014).
73. Hennes, M. et al. Time-resolved XUV absorption spectroscopy and magnetic circular dichroism at the  $NiM_{2,3}$ -edges. *Appl. Sci.* **11**, 325 (2021).
74. Willems, F. et al. Probing ultrafast spin dynamics with high-harmonic magnetic circular dichroism spectroscopy. *Phys. Rev. B* **92**, 220405 (2015).
75. Kfir, O. et al. Generation of bright phase-matched circularly-polarized extreme ultraviolet high harmonics. *Nat. Photonics* **9**, 99–105 (2015).
76. Neufeld, O., Tancogne-Dejean, N., De Giovannini, U., Hübener, H. & Rubio, A. Light-driven extremely nonlinear bulk photogalvanic currents. *Phys. Rev. Lett.* **127**, 126601 (2021).
77. Heinrich, T. et al. Chiral high-harmonic generation and spectroscopy on solid surfaces using polarization-tailored strong fields. *Nat. Commun.* **12**, 3723 (2021).
78. De Giovannini, U., Larsen, A. H. & Rubio, A. Modeling electron dynamics coupled to continuum states in finite volumes with absorbing boundaries. *Eur. Phys. J. B* **88**, 56 (2015).
79. Neufeld, O. & Cohen, O. Background-free measurement of ring currents by symmetry-breaking high-harmonic spectroscopy. *Phys. Rev. Lett.* **123**, 103202 (2019).
80. Sato, S. A. First-principles calculations for attosecond electron dynamics in solids. *Comput. Mater. Sci.* **194**, 110274 (2021).
81. Karczmarek, J., Wright, J., Corkum, P. & Ivanov, M. Optical centrifuge for molecules. *Phys. Rev. Lett.* **82**, 3420–3423 (1999).
82. McMaster, W. H. Polarization and the Stokes parameters. *Am. J. Phys.* **22**, 351–362 (1954).

## ACKNOWLEDGEMENTS

This work was supported by the Cluster of Excellence Advanced Imaging of Matter (AIM), Grupos Consolidados (IT1249-19), SFB925, “Light induced dynamics and control of correlated quantum systems” and has received funding from the European Union’s Horizon 2020 research and innovation program under the Marie Skłodowska-Curie grant agreement No. 860553. The Flatiron Institute is a division of the Simons Foundation. O.N. gratefully acknowledges the generous support of a Schmidt Science Fellowship.

## AUTHOR CONTRIBUTIONS

O.N. conceived and initiated the research project, performed all calculations and analysis presented in the main text, and wrote the first draft. N.T.D., H.H., and U.D.G.,

and A.R. contributed to the data analysis and interpretation. A.R. supervised the project. All authors discussed the results and contributed to the final paper.

## FUNDING

Open Access funding enabled and organized by Projekt DEAL.

## COMPETING INTERESTS

The authors declare no competing interests.

## ADDITIONAL INFORMATION

**Supplementary information** The online version contains supplementary material available at <https://doi.org/10.1038/s41524-023-00997-7>.

**Correspondence** and requests for materials should be addressed to Ofer Neufeld or Angel Rubio.

**Reprints and permission information** is available at <http://www.nature.com/reprints>

**Publisher’s note** Springer Nature remains neutral with regard to jurisdictional claims in published maps and institutional affiliations.



**Open Access** This article is licensed under a Creative Commons Attribution 4.0 International License, which permits use, sharing, adaptation, distribution and reproduction in any medium or format, as long as you give appropriate credit to the original author(s) and the source, provide a link to the Creative Commons license, and indicate if changes were made. The images or other third party material in this article are included in the article’s Creative Commons license, unless indicated otherwise in a credit line to the material. If material is not included in the article’s Creative Commons license and your intended use is not permitted by statutory regulation or exceeds the permitted use, you will need to obtain permission directly from the copyright holder. To view a copy of this license, visit <http://creativecommons.org/licenses/by/4.0/>.

© The Author(s) 2023